2-10-2023

Measurement of Proton Light Yield of Water-based Liquid Scintillator

E. J. Callaghan
University of California - Berkeley

B. L. Goldblum
University of California - Berkeley

J. A. Brown
University of California - Berkeley

T. A. Laplace
University of California - Berkeley

Juan J. Manfredi
Air Force Institute of Technology

See next page for additional authors

Recommended Citation

Callaghan, E. J., Goldblum, B. L., Brown, J. A., Laplace, T. A., Manfredi, J. J., Yeh, M., & Gann, G. D. O. (2023). Measurement of proton light yield of water-based liquid scintillator. The European Physical Journal C, 83(2), 134. https://doi.org/10.1140/epjc/s10052-023-11242-2

Eur. Phys. J. C (2023) 83:134
https://doi.org/10.1140/epjc/s10052-023-11242-2

THE EUROPEAN PHYSICAL JOURNAL C

Regular Article - Experimental Physics

Measurement of proton light yield of water-based liquid scintillator

E. J. Callaghan[1,2,a], **B. L. Goldblum**[2,3], **J. A. Brown**[3], **T. A. Laplace**[3], **J. J. Manfredi**[3,5], **M. Yeh**[4], **G. D. Orebi Gann**[1,2]

[1] Physics Department, University of California at Berkeley, Berkeley, CA 94720, USA
[2] Nuclear Science Division, Lawrence Berkeley National Laboratory, Berkeley, CA 94720, USA
[3] Department of Nuclear Engineering, University of California at Berkeley, Berkeley, CA 94720, USA
[4] Chemistry Division, Brookhaven National Laboratory, Upton, NY 11973, USA
[5] Present Address: Department of Engineering Physics, Air Force Institute of Technology, Wright-Patterson Air Force Base, OH 45433, USA

Received: 7 October 2022 / Accepted: 23 January 2023

Abstract The proton light yield of liquid scintillators is an important property in the context of their use in large-scale neutrino experiments, with direct implications for neutrino-proton scattering measurements and the discrimination of fast neutrons from inverse β-decay coincidence signals. This work presents the first measurement of the proton light yield of a water-based liquid scintillator (WbLS) formulated from 5% linear alkyl benzene (LAB), at energies below 20 MeV, as well as a measurement of the proton light yield of a pure LAB + 2 g/L 2,5-diphenyloxazole (PPO) mixture (LABPPO). The measurements were performed using a double time-of-flight method and a pulsed neutron beam from the 88-Inch Cyclotron at Lawrence Berkeley National Laboratory. The proton light yields were measured relative to that of a 477 keV electron. The relative proton light yield of WbLS was approximately 3.8% lower than that of LABPPO, itself exhibiting a relative proton light yield 15–20% higher than previous measurements of an analogous anoxic sample. The observed quenching is not compatible with the Birks model for either material, but is well described with the addition of Chou's bimolecular quenching term.

1 Introduction

Neutrinos provide a gateway to improved understanding of basic physics, though their fundamental nature remains unknown. Liquid scintillators have been a mainstay for experimental neutrino physics, from the Cd-loaded toluene medium employed by Reines and Cowen [1] to the linear alkylbenzene (LAB) based systems of today [2,3]. While liquid scintillators demonstrate high efficiency for the conversion of particle kinetic energy into detectable light, the isotropic emission of scintillation photons makes generic reconstruction of neutrino directionality notoriously difficult.

Water-based liquid scintillator (WbLS) [4] has emerged as a versatile detection medium for large-volume neutrino detectors, capable of leveraging both the Cherenkov and scintillation light, and is a candidate material to be deployed in upcoming liquid-phase detectors including ANNIE [5], AITNEO [6], and THEIA [7]. It is composed of organic liquid scintillator encapsulated in micelles and dispersed in a water solvent, which has the advantage of providing increased light yield relative to traditional water-based detectors with only nominal increase in cost, while retaining a relatively clear Cherenkov signal. Prior measurements of the scintillation emission spectrum, light yield, and temporal response, as well as demonstrated separation between Cherenkov and scintillation photon populations [8–10] offer the possibility of vertex reconstruction comparable to that achieved with pure liquid scintillator but with improved directional sensitivity [11]. Given this, WbLS holds promise for enabling new hybrid neutrino detector design concepts, which admit robust directional reconstruction with lower detection thresholds.

The advantages offered by WbLS extend the reach of neutrino detectors to several fundamental science goals [7]. The relatively low cost allows for the construction of larger detectors, with the low energy threshold enabling large-scale searches for neutrinos from the Diffuse Supernova Neutrino Background (DSNB) and proton decay, for example, and directional reconstruction capabilities offering enhanced measurements of low energy solar neutrinos. The relative abundance of Cherenkov light allows for high-precision ring imaging, which improves particle-identification capability,

[a] e-mail: ejc3@berkeley.edu (corresponding author)

Published online: 10 February 2023

improving sensitivity in e.g., long-baseline oscillation measurements.

In addition to the basic science applications, recent advances in antineutrino physics technologies have motivated considerable interest in WbLS for neutrino-based reactor monitoring. Through measurement of the fission neutrino signal from a nuclear reactor, it is theoretically possible to discern the reactor power level and isotopic composition of the fuel, important proliferation indicators for nuclear security applications [12]. Given the low neutrino interaction cross section, the accurate prediction of background signals arising from ambient radioactivity is critical. For example, fast neutrons from cosmogenic muon interactions represent an important source of background for inverse β-decay (IBD) measurements. Internal radioactive contaminants, e.g., neutrons produced via the $^{13}C(\alpha, n)^{16}O$ reaction, may represent additional background contributors [13]. Fast neutrons primarily generate light in scintillating media via np elastic scattering before capturing. As such, measurement of the proton light yield (PLY) of WbLS is essential in distinguishing neutron interactions from true IBD events, as it allows the kinetic energy of recoil protons to be determined, enabling signal and background to be distinguished spectrally.

This work presents the first measurement of the proton light yield of WbLS, loaded at the level of 5% scintillator concentration. A measurement of LAB with 2 g/L 2,5-diphenyloxazole (PPO), henceforce denoted LABPPO, was also conducted to serve as a fiducial reference – though nondilute mixtures of LAB and PPO form the bases of target materials in several large-volume neutrino detectors [14–17], and thus the PLY of this pure scintillator is of its own merit. Section 2 provides a description of the experimental setup and associated electronics configuration. In Sect. 3, the analytic methods are described, including the calibrations of the electronics and energy reconstruction, the extraction of the proton light yield, and tests of quenching model compatibility. Section 4 presents the measured PLY relations of WbLS and LABPPO in the energy range of 2–20 MeV along with ionization quenching model fits. Concluding remarks are given in Sect. 5.

2 Experimental setup

A broad spectrum neutron beam was produced by impinging a 33-MeV $^2H^+$ beam onto a 3-mm-thick Be target at the 88-Inch Cyclotron at Lawrence Berkeley National Laboratory [18]. The LABPPO and WbLS samples to be characterized were independently placed in beam, about 7 m downstream of the breakup target. Eleven auxiliary detectors, filled with EJ-309 [19], an organic liquid scintillator with pulse-shape-discrimination (PSD) capabilities, were positioned out of beam to detect forward-scattered neutrons from the target scintillator, each at a unique scattering angle. A schematic diagram of the experimental setup is shown in Fig. 1. The detector geometries employed for the two measurements are provided in Table 1. The geometry was established using laser-based coordinate measurements, assigning a 1 cm uncertainty to each measurement except the z-position of the breakup target, which is known to 5 mm.

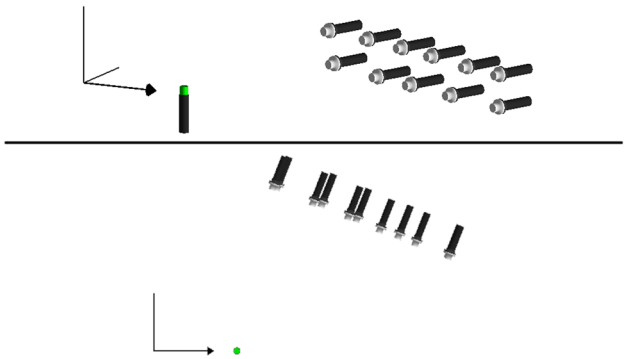

Fig. 1 Experimental setup for proton light yield measurements. The neutron beam travels along the axis designated with an arrow to the target scintillator cell, shown in green. Eleven auxiliary detectors are positioned at forward scattering angles with respect to the incoming neutron beam. The upper face and side walls of the target cell, highlighted in green, was wrapped with Teflon tape; the lower face was unwrapped and optically coupled to a PMT. Top and bottom panels show the experimental geometry from lateral and from-above vantage points

Further details of the experimental hall, Be target, and auxiliary detector shielding can be found in [20]. For 33-MeV deuterons, the neutron beam has a broad energy distribution dominated by breakup neutrons centered at approximately 15 MeV, and ranging continuously from the slow spectral region up to 37.4 MeV (the incident deuteron energy plus the reaction Q-value) due to compound and pre-equilibrium reactions. Further discussion and measurements of comparable beams can be found in [21–24]. For each sample, data were acquired over a period of approximately 11 h of beam running with a current of approximately 55 nA. The period between beam extractions was approximately 111 ns.

The LABPPO and WbLS target scintillators were contained in cylindrical quartz crucibles, of dimensions 50 mm diameter by 50 mm tall and 1 mm in wall thickness. A quartz disk of the same thickness was used to seal the open face using a two-part epoxy. The side wall and sealed face of the cells were wrapped in no less than 10 layers of polytetrafluoroethylene (PTFE) tape to improve internal reflectivity, and thus light collection. The remaining transparent face was optically coupled to a Hamamatsu H1949-51 photomultiplier tube (PMT) using EJ-550 silicone grease. The sealed cells, both before and after wrapping with PTFE, are shown in Fig. 2.

Table 1 Distances between various experimental apparatus, and nominal scattering angles associated with each auxiliary detector

	Channel	LABPPO		WbLS	
		Distance [cm]	Scattering angle [°]	Distance [cm]	Scattering angle [°]
Breakup to target		721.3 ± 1.4	–	716.6 ± 1.4	–
Target to	2	133.8 ± 1.8	80.0 ± 1.9	134.2 ± 1.8	78.0 ± 1.9
	3	131.7 ± 2.1	65.0 ± 2.0	133.2 ± 2.1	63.1 ± 2.0
	4	137.6 ± 2.2	52.2 ± 2.0	140.0 ± 2.1	50.5 ± 1.9
	5	148.1 ± 2.2	41.9 ± 1.9	151.1 ± 2.1	40.4 ± 1.8
	6	165.4 ± 2.1	32.3 ± 1.7	168.9 ± 2.0	31.2 ± 1.7
	7	184.9 ± 2.0	25.1 ± 1.6	188.7 ± 1.9	24.2 ± 1.5
	9	133.0 ± 1.7	78.1 ± 1.9	134.1 ± 1.6	76.2 ± 2.0
	12	132.7 ± 1.9	61.4 ± 2.0	135.1 ± 1.9	59.7 ± 2.0
	13	139.6 ± 2.0	48.7 ± 2.0	142.7 ± 1.9	47.3 ± 1.9
	14	156.2 ± 2.0	35.9 ± 1.8	160.0 ± 1.9	34.9 ± 1.8
	15	183.7 ± 1.8	24.4 ± 1.6	187.9 ± 1.8	23.8 ± 1.5

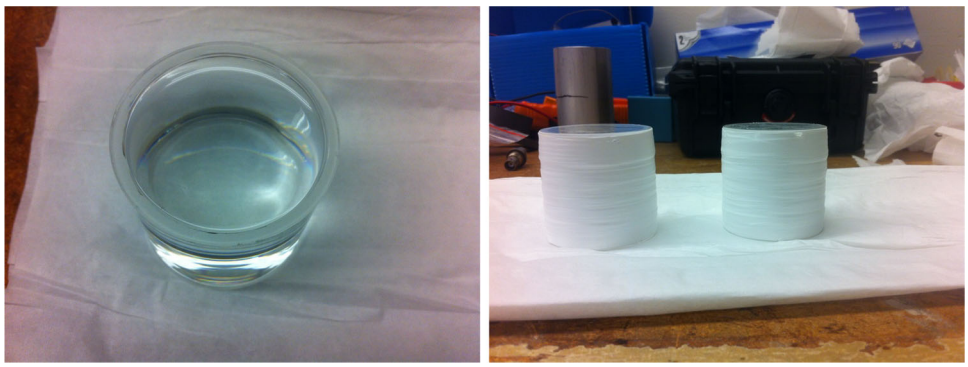

Fig. 2 (Left) Sealed target cell containing LABPPO before wrapping with PTFE tape. (Right) Both target cells after wrapping in PTFE

The scintillator cells of the auxiliary detectors were right cylinders of diameter and height 50.8 mm, constructed of a thin aluminum housing and filled with EJ-309 [19], and were each coupled to a PMT via a borosilicate glass window and EJ-550 silicone grease. All PMTs used in these measurements were obtained from Hamamatsu Photonics (either Type No. 1949-50 or 1949-51), and were negatively biased using either a CAEN R1470ET or CAEN NDT1470 power supply.

The data acquisition system triggered on a coincidence between the target PMT and any of the auxiliary detectors within a 400 ns coincidence window. Upon triggering, digital waveforms of a total length of 800 ns from all channels, as well as a waveform digitizing a sinusoidal RF control signal provided by cyclotron operations, were recorded using a CAEN V1730 500 MS/s digitizer. The scintillator signal timing was determined using the CAEN digital constant fraction discrimination algorithm, with a 75% fraction and a 4 ns delay. The timing pickoff for the cyclotron RF signal was determined using leading-edge discrimination.

3 Analysis methods

Waveforms from the target and auxiliary detectors were integrated to compute the charge collected in the associated PMT in units of summed analog-to-digital-converter readings (adc), after correcting for nonlinearity of the target PMT as described in Sect. 3.1. All uses of the term "charge" in this work refer to such waveform integrals, and are proportional to the number of photons detected by the relevant PMT. Waveforms in the target detectors were integrated for 140 ns to ensure collection of $\geq$ 95% of the observed charge. For the auxiliary detectors, waveforms were integrated for 300 ns, and a PSD-metric was obtained by calculating the ratio of the charge of the prompt region corresponding to the first 30 ns of the waveform, to the delayed region between 30 and 260 ns from the start of the waveform, providing good separation between γ-ray and neutron signals for high-charge producing events. For coincident events, the high-level observables are the charge and timing for the target and auxiliary detectors, a PSD-metric for the auxiliary detector, and a timestamp

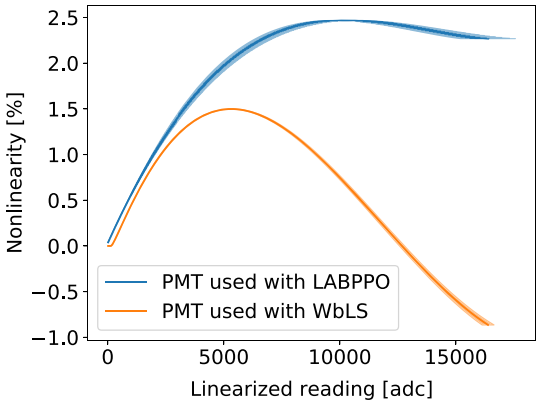

Fig. 3 Deviation of output current from linear operation of the PMTs used in this measurement, as biased during runtime operations. The blue and orange curves correspond to the PMTs mounted to the LABPPO and WbLS samples, respectively. The abscissa spans the full scale range of the employed digitizer. The uncertainty bands are scaled by a factor of 20 for visualization

corresponding to the cyclotron RF signal. To measure the PLY as a function of energy, a conversion between charge in the target PMT and light produced by the sample must be established, γ and neutron interactions distinguished, and the energy deposited by neutron interactions reconstructed from the available timing and geometric information. The methods employed herein were originally introduced in [25,26] and are further detailed below.

3.1 PMT linearity correction

A nonlinearity correction for the two PMTs coupled to the measurement samples was performed using the method of Friend et al. [27]. In brief, each PMT was placed in the view of two LEDs with peak wavelength 405 nm [28], which were flashed both independently and in coincidence, thus recording the PMT response to two independent fluxes, as well as the response to the summed flux. By repeating this procedure over a range of fluxes spanning the range of the digitizer used in this measurement, the deviation from linear operation was computed. The measured nonlinearities, interpreted as quartic polynomials, are shown in Fig. 3 as a function of the pulse amplitude. The nonlinearity correction was applied on a sample-by-sample basis to waveforms collected both during reference charge calibration and beam running.

3.2 Reference charge calibration

To establish a measurement unit proportional to the number of scintillation photons, a reference charge is defined and serves as a calibration. In this work, the reference charge is that associated with a 477 keV electron, evaluated using the Compton edge of the 662 keV γ ray following ^{137}Cs decay. Calibration data were collected using ^{137}Cs (662 keV) and ^{207}Bi (1.770 MeV) sealed sources, as well a ^{24}Na (2.754 MeV) source created by beam-activation of a sample of natural aluminum, placed at distances $\geq$ 10 cm from the center of each target scintillator cell. Because beam operation was required to produce the sample of ^{24}Na, this source was not available before irradiation of the LABPPO sample. For each other source used with the LABPPO scintillator, and for all sources used with the WbLS, calibration data were taken both before and after irradiation. The ^{207}Bi and ^{24}Na sources were used to quantify the systematic uncertainty on the reference charge, and facilitate comparisons with other measurements performed with different calibration schemes.

The charge associated with the Compton edge, or the Compton charge, was determined by fitting a model to the measured calibration data. The model consists of an electron energy deposition spectrum following γ-ray interactions in the scintillator, generated using the `GEANT4` simulation toolkit [29], convolved with a three-parameter system resolution function [30] as well as a power-law background term [31]. A linear charge response was applied to the experimental data to convert the measured charge in units of summed adc, Q, to that associated with a given electron recoil energy, E. The energy-charge relation is $E = aQ+b$, which assumes that the electron light yield is approximately linear in the energy range of interest, with b accounting for potential nonlinearity at lower energies. The minimization was performed using the SIMPLEX and MIGRAD algorithms from the ROOT Minuit2 package [32].

For each target scintillator, the measured calibration data before and after neutron irradiation were fit with the corresponding charge model independently, with the offset term, b, fixed to zero. The resulting Compton charges are reported in Table 2 for each γ-ray source, along with the statistical uncertainty, determined from the parameter uncertainty on a, and systematic uncertainty stemming from the uncertainties in the background shape and electron light linearity, described in detail below.

The systematic uncertainty on the Compton charge is computed as the standard deviation of the Compton charge determined using all available combinations of pairs and triplets of calibration γ rays. Simultaneous fits to multiple Compton edges were performed without any constraint on b, the value of which provides information about low-energy electron light nonlinearity. For LABPPO, $b = (34.71 \pm 1.24)$ keV, and for the WbLS, $b = (185.3 \pm 4.0)$ keV, where the uncertainty on b is given by the standard deviation of the values obtained by fitting all available combinations of pairs and triplets. The difference in b for LABPPO and the WbLS can be attributed, in part, to the larger relative contribution of Cherenkov-to-scintillation light in WbLS compared to LABPPO, and should be taken into account when comparing to quenching measurements obtained using different γ-ray

Table 2 Compton charges for both LABPPO and WbLS. The first uncertainty corresponds to the statistical uncertainty obtained from parameter fitting. The second uncertainty corresponds to the standard deviation of the Compton charge determined using simultaneous fits of multiple calibration spectra (i.e., all combinations of pairs and triplets)

Source	Compton edge energy [keV]	Compton charge [adc]	
		LABPPO	WbLS
^{137}Cs	477	$2525.4 \pm 1.3 \pm 21.2$	$2131.9 \pm 2.6 \pm 53.9$
^{207}Bi	1547	$8617.0 \pm 22.8 \pm 13.7$	$9741.2 \pm 82.8 \pm 94.7$
^{24}Na	2520	$14219.5 \pm 9.3 \pm 44.5$	$16795.5 \pm 15.7 \pm 71.5$

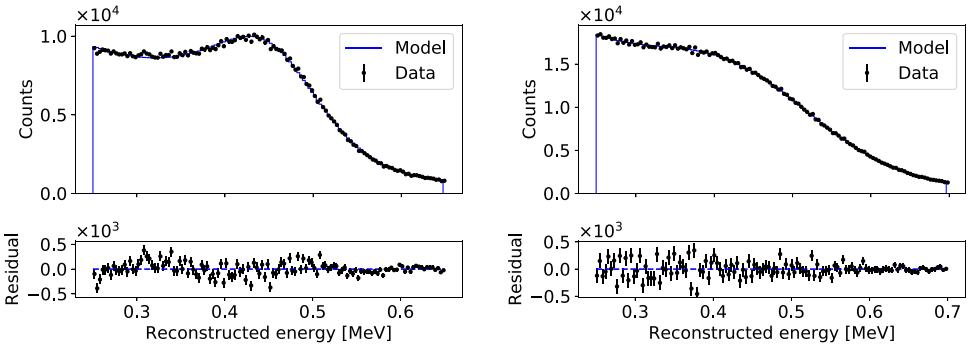

Fig. 4 Best fit charge models compared to LABPPO (left) and WbLS (right) calibration data using a ^{137}Cs source

sources for light calibration. The best-fit charge models are compared to the ^{137}Cs data in Fig. 4.

The gain stability of the target PMTs was investigated by chronologically partitioning the full beam dataset for each scintillator into 10 distinct datasets and analyzing each separately. No systematic trends or significant fluctuations were observed in the PLY results. A strong ambient γ-ray background was present in the experimental hall due to activation from previous experiments. The presence of this background can introduce bias in the determination of the Compton charge, and the associated systematic uncertainty was quantified by comparing the results of calibration both before and after data collection, for which data were taken in different locations in the experimental hall. The difference in the ^{137}Cs Compton charge before and after irradiation is 1.8 and 1.5% for LABPPO and WbLS, respectively. Smaller differences were observed for the ^{207}Bi lines (0.1 and $-$ 0.3%) and the ^{24}Al data (0.6%), which are each in a higher energy region where the background contribution is less significant.

3.3 Auxiliary detector particle identification

The 11 auxiliary detectors located at forward scattering angles are filled with EJ-309 [19], a commercial liquid scintillator with established particle-identification (PID) capabilities achieved via PSD, in this case exploiting that γ-ray pulses have a higher ratio of prompt to delayed light relative to neutron pulses. For each auxiliary detector, a constraint on the total charge collected is chosen to reject events in the low-charge region where the distributions of PSD values from pulses originating from neutron and γ-ray interactions overlap. These constraints are then imposed on beam data, after which the PSD metric, i.e., the ratio of delayed to prompt charge, is binned and fit with an empirical normal-plus-lognormal form, where the former term models the distribution of γs and the latter neutrons. After performing the fit, an optimal PSD value for distinguishing between the two components is determined by minimizing the neutron contamination of γ selection, with the resultant purity above 98% for high-charge events.

3.4 Energy reconstruction

The neutron beam employed in this work has a broad energy distribution, as discussed in Sect. 2. While advantageous in allowing simultaneous measurement over a broad energy range, this necessitates event-wise energy reconstruction, which is achieved via two time-of-flight measurements that translate to the neutron energy both before and after interacting with the target scintillator volume. The detection of the scattered neutron in an auxiliary detector establishes a scattering angle which, for single elastic scatters, kinematically overconstrains the system. For single scatters, the proton energy, E_p, is reconstructed in this work using the incident neutron energy, E_n, and scattering angle, θ:

$$E_p = E_n \sin^2\theta. \quad (1)$$

This method generally provides the best available resolution on the proton recoil energy, owing to the relatively long neutron flight path from production to target. That it is optimal

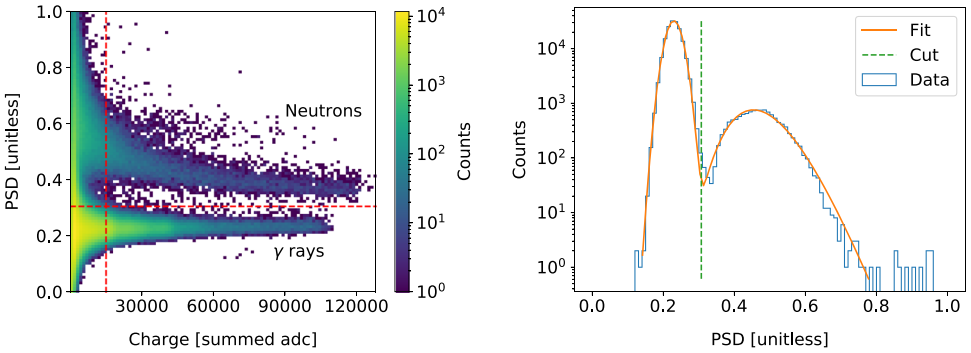

Fig. 5 (Left) PSD metric vs charge collected in the PMT for beam events in an example auxiliary detector, showing separation between neutrons and γ rays at high charge. (Right) Projection onto the PSD-axis for events with charge above 15,000 adc, along with a normal-lognormal fit and subsequently optimized discrimination threshold

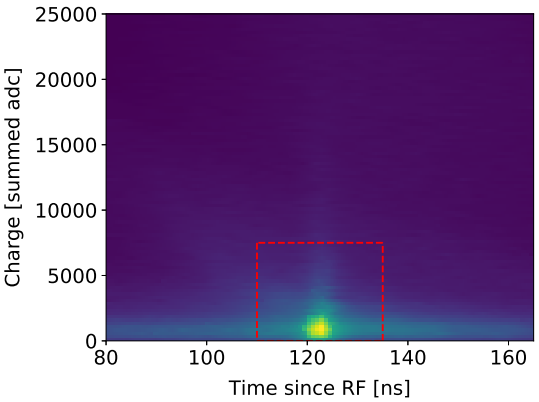

Fig. 6 Charge collected in target PMT vs uncalibrated time since beam extraction during LABPPO data collection. Low energy beam-correlated γ rays appear as an isochronic population at low charge. The selection window is illustrated using the red dashed lines

for the current geometry was confirmed both by propagating time-of-flight and interaction-point uncertainties analytically, and using simulations similar to those described in [26].

To perform energy reconstruction, the time-of-flight (TOF) measurements are calibrated to correct for cable and system delays. A calibration is performed to determine time differences between interactions in the breakup target and the measurement cell (the "incoming TOF"), and from the measurement cell to each of the 11 auxiliary detectors (the "outgoing TOF"). In all cases, the calibration is achieved by selecting on beam-correlated γ rays and comparing the measured clock differences to the true TOF given the known speed of light and measured detector positions. Selection of γ rays for the outgoing TOF is achieved by exploiting the PSD capabilities of EJ-309, as exemplified in Fig. 5; γ-ray selection for the incoming TOF is achieved by selecting low-charge events in the target cell in a given time window, as exemplified in Fig. 6. Efforts to apply PSD-based neutron/γ-ray discrimination using the target scintillators were not fruitful, likely attributable to the dissolved oxygen content.

The resultant distributions of measured γ-ray time differences are shown in Figs. 7 and 8 for the incoming and outgoing TOF, respectively. Each distribution is fit with an empirical function comprised of a Gaussian signal term and a polynomial background term. For the outgoing TOF, the background is modeled using a linear term and is dominated by uncorrelated γ rays uniformly distributed in time; a nonzero slope is allowed to account for a potential asymmetry around the γ-ray population introduced by beam-correlated contamination. For the incoming TOF, there is an additional background of beam-correlated neutrons from previous beam extractions, which have a nontrivial timing structure associated with their energy spectra, and thus a quadratic background term is allowed. The uncertainty in any measured neutron TOF, which propagates to uncertainty in proton recoil energy, is determined both by the uncertainty on the mean of the Gaussian and its width. The width of the incoming TOF is dominated by the temporal profile of the beam pulse. All calibration uncertainties are significantly below 1%, and the best-fit standard deviations are provided in Table 3. The relatively poor quality of the fit to the incoming TOF data may be due to the relatively high background rate and shortcomings of the single-Gaussian signal model which in reality is modified by a number of effects, notably the perturbations to the beam due to multiple extraction from the main cyclotron ring. As neutron energy reconstruction is performed under the single beam extraction hypothesis, the relevant quantity for the incoming TOF calibration is the centroid of the γ-ray population, which is adequately described using the empirical model.

There is ambiguity as to which beam extraction a given neutron detected in the target cell was produced from, associated with the relatively short cyclotron extraction period of 111 ns. For comparison, the time for a 10 MeV neutron to travel from the production Be target to the target scintillator cell is approximately 165 ns. A measured incoming TOF can thus be interpreted only as measured modulo the cyclotron period. This ambiguity is resolved by kinematically reconstructing an expected incoming TOF using the outgoing TOF and the known scattering angle. If there is a multiple of the cyclotron period by which the measured and reconstructed incoming TOFs agree to within less than

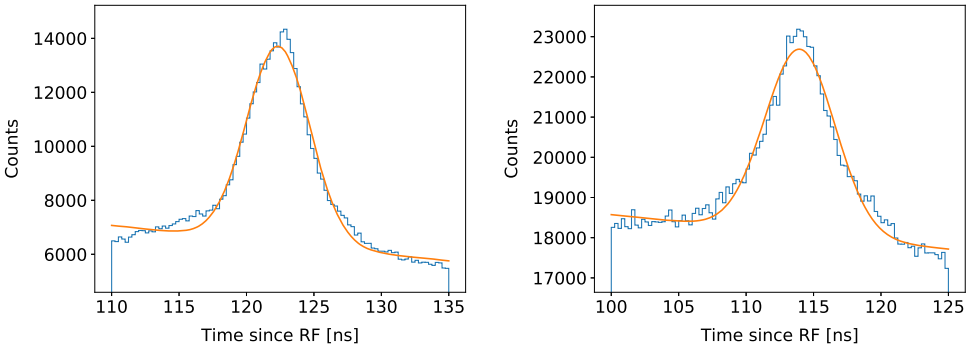

Fig. 7 Distribution of measured time differences between the cyclotron RF signal and γ-ray events in the measurement sample, with empirical fit overlaid, during LABPPO (left) and WbLS (right) data collection

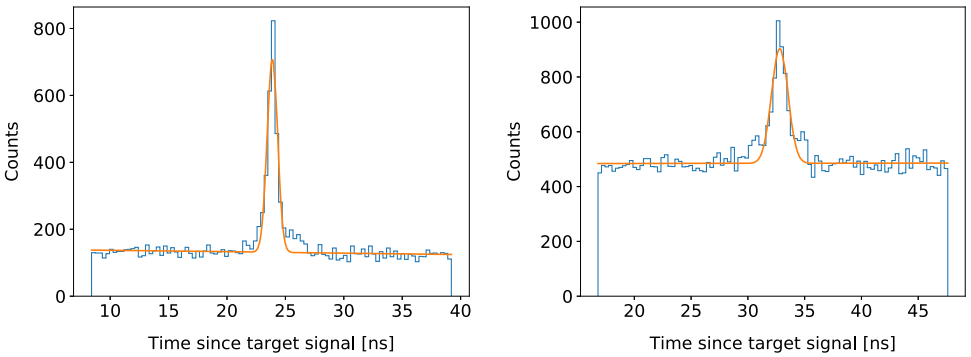

Fig. 8 Distribution of measured time differences between γ-ray events in the measurement sample and a representative auxiliary detector, with empirical fit overlaid, during LABPPO (left) and WbLS (right) data collection. The data for each material is shown for channel 2, which is located at nominal scattering angles of 80° and 78°, respectively

Table 3 Standard deviations of best-fit Gaussian models for TOF distributions of all neutron trajectories, in both the LABPPO and WbLS datasets. Uncertainties on all Gaussian parameters are significantly below 1%

	Channel	Standard deviation [ps]	
		LABPPO	WbLS
Incoming	–	2348.2	2608.8
Outgoing	2	406.6	811.1
	3	431.7	914.1
	4	448.5	727.9
	5	430.3	943.4
	6	399.9	896.3
	7	420.7	899.5
	9	502.8	1019.9
	12	403.0	828.8
	13	379.9	914.0
	14	464.1	730.8
	15	423.4	799.9

10 ns, the event is considered kinematically consistent and the ambiguity resolved. An example distribution showing the charge collected in the target PMT and the resolved incoming time-of-flight is shown in Fig. 9.

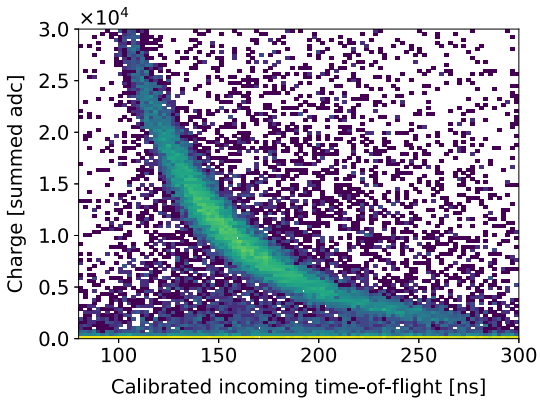

Fig. 9 Charge collected in the target PMT vs incoming time-of-flight for neutron-like events which were tagged in channel 5

3.5 Proton light yield extraction

Signal events are selected by applying the kinematic consistency criteria described in Sect. 3.4 and by selecting neutron events via PID in each auxiliary detector. Two-dimensional distributions of charge and deposited energy for the selected events are shown in Fig. 10. To extract the PLY relation, events are partitioned into energy bins, the widths of which are guided by the resolution of single-scatter energy reconstruction, calculated using the TOF calibrations of Sect. 3.4 and geometry given in Table 1. A representative charge is assigned to each bin by fitting its population of charge values with an empirical distribution comprised of a Gaussian signal term and two exponential background terms. The centroid of each Gaussian is the representative charge for a given energy bin and, relative to the reference charge defined in

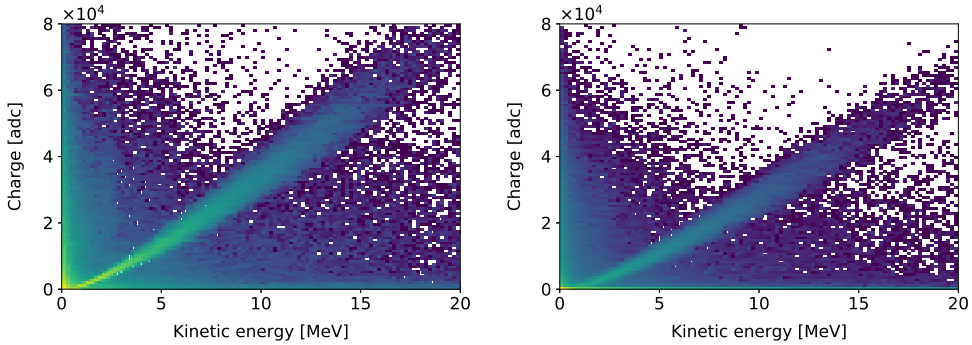

Fig. 10 Charge collected in the target PMT vs energy deposited in the scintillator for kinematically-consistent events in LABPPO (left) and WbLS (right) data

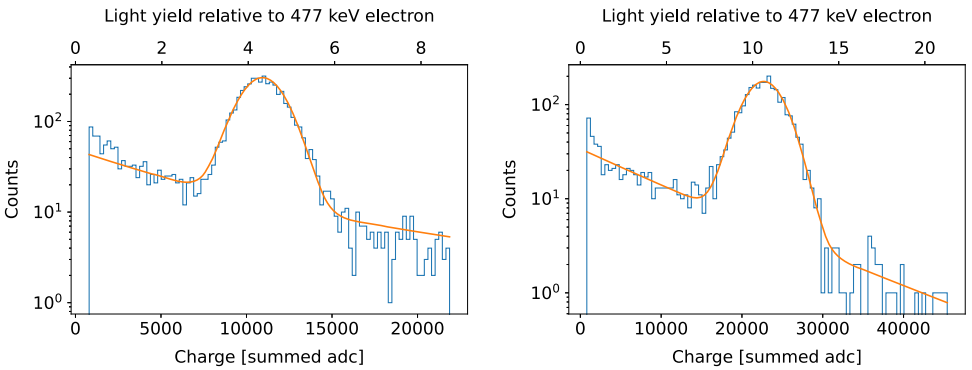

Fig. 11 Distributions of charge values for kinematically consistent events, with empirical fits overlaid, of individual proton energy bins: 4.0–4.5 MeV events in LABPPO (left) and 8.0–9.0 MeV events in WbLS (right)

Sect. 3.2, establishes the scale of the relative proton light yield observed. Examples of such fits are shown in Fig. 11.

The fit is formulated using an unbinned maximum likelihood method, and performed using a two-step minimization wherein a global minimization based on a simulated-annealing technique (provided by `SciPy` [33]) is followed by a simplex-based local minimization (provided by `NLopt` [34]). Uncertainties are computed using a resampling technique: the statistical uncertainty is computed via bootstrapping [35], wherein the dataset is repeatedly refit under resampling with replacement, and the total uncertainty, which includes systematic effects, is computed similarly, but with analysis parameters which act as sources of uncertainty simultaneously resampled at each iteration. The sources of systematic uncertainty considered include the experimental geometry and timing calibrations: the coordinates of the breakup target, measurement cell, and each auxiliary detector, and the calibration value for each time-of-flight measurement. Each are sampled from normal distributions centered on their nominal values, with standard deviations equal to the associated uncertainties. For each trial, energy reconstruction is performed and each energy bin is refit to extract a representative charge. This procedure generates a non-diagonal covariance matrix due to correlations between energy bins, which stem from the different energy spectra associated with different auxiliary detectors.

3.6 Modeling ionization quenching

Ionization quenching refers to a reduction in scintillation output resulting from high excitation and ionization densities produced by a recoiling ion in a scintillating medium. Birks proposed the first phenomenological description for organic scintillators in 1951 [36] and this model remains widely used in the literature today. For an ion slowing down along a distance x in the scintillating material, the amount of scintillation light produced, L, is given by:

$$\frac{\mathrm{d}L}{\mathrm{d}x} = \frac{S\,\frac{\mathrm{d}E}{\mathrm{d}x}}{1 + kB\,\frac{\mathrm{d}E}{\mathrm{d}x}}, \tag{2}$$

where $\mathrm{d}E/\mathrm{d}x$ is the stopping power of the ion in the scintillating medium, S establishes the conversion between light produced and energy deposited in the limit of an unquenched system, and kB, termed the Birks constant, introduces nonlinearity characteristic of ionization quenching. Discrepancies have been observed between the Birks model and measured PLY data, particularly below 1 MeV, for a variety of organic scintillators [13,37,38]. More recently, it has been shown that the model fails to accurately describe the PLY of four different samples for energies above 1 MeV when lower energy data are considered [39]. Chou extended the model by introducing a bimolecular quenching term [40] which contributes quadratically with the stopping power:

$$\frac{\mathrm{d}L}{\mathrm{d}x} = \frac{S\frac{\mathrm{d}E}{\mathrm{d}x}}{1 + kB\frac{\mathrm{d}E}{\mathrm{d}x} + C\left(\frac{\mathrm{d}E}{\mathrm{d}x}\right)^2}. \tag{3}$$

Using either model, the total photon yield for a fully stopped ion can be found by numerically integrating the quenching relation using a table of stopping powers.

Quenching parameters are extracted by fitting each model to the measured PLY data via χ^2 minimization, with χ^2 defined as:

$$\chi^2 = \sum_{i,j} \Delta_i H_{ij} \Delta_j, \tag{4}$$

where Δ_i is given by:

$$\Delta_i = \left(Y_i - f\left(E_i; S, kB, C\right)\right). \tag{5}$$

Here, E_i and Y_i are the centroid and relative PLY value of the ith proton energy bin, respectively; $f\left(E; S, kB, C\right)$ denotes the integration of the model up to energy E; and H is the inverse of the covariance matrix of the dataset under consideration. Stopping power tables were generated using the Stopping Range of Ions in Matter (SRIM) software package [41], in which the stopping power of a compound material is calculated as a linear combination of those of its atomic constituents, as suggested by [42]. For table-defined energies E, the integral is performed using the trapezoidal rule. For non-table-defined energies, the yield is computed by linearly interpolating between adjacent table-defined yields. Parameter uncertainties and correlations are computed from the covariance matrix.

4 Results

4.1 Proton light yield

The light yields of LABPPO and WbLS as a function of proton recoil energy are shown in Fig. 12 and listed in Tables 4 and 5, respectively. The horizontal error bars denote the energy bin widths and do not represent uncertainty. The relative PLY of WbLS is consistently lower than that of LABPPO by 3.8%, although some energy bins below 9.5 MeV are consistent to within $1\,\sigma$. Systematic uncertainty generally dominates over statistical uncertainty, and is driven by the uncertainties on the experimental geometry tabulated in Table 1.

Previous PLY measurements of several LABPPO formulations were performed by von Krosigk et al. using a neutron beam at the Physikalisch-Technische Bundesanstalt (PTB) [43]. The PTB measurement for a deoxygenated 2 g/L LABPPO scintillator is also shown in Fig. 12. The relative PLY data are systematically lower than the LABPPO PLY obtained in this work by 15–20%. A discrepancy between the PLY of the two samples is not unexpected as the LABPPO measured at PTB was deoxygenated via bubbling with gaseous argon, which removes molecular oxygen, whereas the sample measured in this work was not. Such deoxygenation has been shown to impact ionization quenching [44,45], though the relative proton light yield would be expected to decrease in aerated samples, not increase as is observed here, due to the differential impact of oxygen quenching of triplet states given the higher fraction of delayed light for proton recoils relative to electrons.

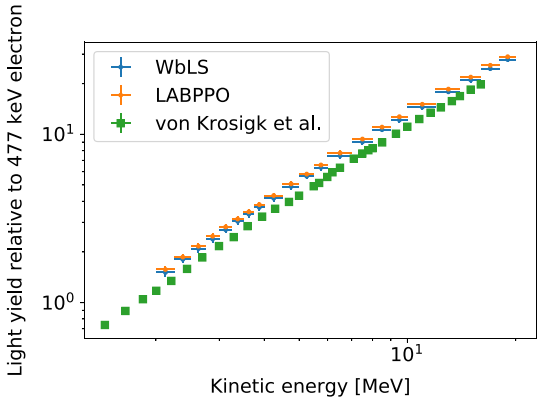

Fig. 12 Proton light yield of LAB + 2 g/L PPO and 5% WbLS, relative to that of a 477 keV electron. A previous measurement of deoxygenated 2 g/L LABPPO by von Krosigk et al. [43] is overlaid

There are a number of factors that can potentially explain this discrepancy. Different integration lengths used in waveform processing can lead to significant discrepancies in relative proton light yields [25,46]. This is due to differences in the scintillation temporal profiles of electrons and protons, as well as potential variation in the proton pulse shape with recoil energy: use of an integration length that is too short results in a pulse integral that is not proportional to the total number of scintillation photons. The integration length used in this work is 140 ns, which was chosen to ensure that $> 95\%$ of the light was collected. The integration length used in the PTB measurement is not reported in [43].

The reference charge calibration also represents a potential source of bias. The electron light yield of LABPPO has been shown to deviate from linearity below ~ 400 keV [47]. The PTB group used multiple γ-ray sources but assumed electron light linearity, equivalent to fixing the offset parameter $b = 0$. For LABPPO, the multi-source calibration performed in this work leads to an offset parameter, $b = 34.7 \pm 1.2$ keV, indicative of electron light nonlinearity. The average charge per unit energy can be calculated for the single Compton edge fits described in Sect. 3.2. This charge per unit energy is 5.2% greater when using the 1547 keV Compton edge from ^{207}Bi compared to the 477 keV Compton edge from ^{137}Cs; this value is 6.6% greater if the 2520 keV Compton edge from ^{24}Na is used.

Finally, the edge characterization method employed in [43] to extract the PLY is known to be subject to bias [25,48].

Table 4 Light yield of proton recoils, relative to that of a 477 keV electron, in LAB + 2 g/L PPO, and associated uncertainties (from left to right): statistical uncertainty, uncertainty on reference charge, and total uncertainty including systematic effects. A correlation matrix of the per-bin uncertainties is available upon request

Energy range [MeV]	Relative LY	Stat. uncertainty [%]	Ref. uncertainty [%]	Total uncertainty [%]
2.00–2.25	1.57	±0.27	±0.84	±4.85
2.25–2.50	1.87	±0.25	±0.84	±4.51
2.50–2.75	2.16	±0.24	±0.84	±4.32
2.75–3.00	2.48	±0.25	±0.84	±4.47
3.00–3.25	2.82	±0.24	±0.84	±4.00
3.25–3.50	3.14	±0.25	±0.84	±3.89
3.50–3.75	3.46	±0.25	±0.84	±3.82
3.75–4.00	3.82	±0.26	±0.84	±3.55
4.00–4.50	4.33	±0.20	±0.84	±3.60
4.50–5.00	5.08	±0.19	±0.84	±3.19
5.00–5.50	5.80	±0.19	±0.84	±3.17
5.50–6.00	6.57	±0.19	±0.84	±2.96
6.00–7.00	7.74	±0.16	±0.84	±2.84
7.00–8.00	9.38	±0.17	±0.84	±2.59
8.00–9.00	11.05	±0.20	±0.84	±2.68
9.00–10.00	12.72	±0.21	±0.84	±2.27
10.00–12.00	15.09	±0.19	±0.84	±1.99
12.00–14.00	18.56	±0.25	±0.84	±1.91
14.00–16.00	21.86	±0.34	±0.84	±1.89
16.00–18.00	25.71	±0.49	±0.84	±1.87
18.00–20.00	28.84	±0.76	±0.84	±1.75

In particular, the importance of neutron response modeling to the PTB measurement necessitates the need to extrapolate the light yield curve to lower energies in order to properly account for multiple neutron scatters, whereas the kinematic consistency and signal extraction methods employed in this work are model independent.

4.2 Model compatibility

Figure 13 shows the best-fit quenching models for the LABPPO and WbLS relative proton light yield data obtained using the Birks and Chou parameterizations (see Eqs. (2) and (3), respectively). The best-fit model parameters are listed in Table 6. The Chou model provides a better fit for each material and significant deviations are observed for the Birks fit of the WbLS data below 3 MeV proton recoil energy. The parameter correlation between S and kB in the Birks model is 87.2 and 87.4% for the LABPPO and WbLS datasets, respectively. Correlation matrices associated with the Chou model are provided in Table 7.

The PLY of LAB + 2 g/L PPO (+ 15 mg/L bis-MSB, a secondary fluor) were measured using a proton beam at the NASA Space Radiation Laboratory at Brookhaven National Laboratory, and fit with Birks' law in [49]. The reported best-fit Birks' constant of $kB = (7.0 \pm 0.1)$ cm/GeV) is consistent with the present result, although it should be noted that the Brookhaven measurement was performed at energies above 20 MeV. The PTB study investigated ionization quenching in LABPPO using the Chou model [43]. In that work, scintillation light was quantified using an electron-equivalent energy in units of MeVee/MeV, and S was fixed to a value of 1 MeVee/MeV. In this work, scintillation light was determined relative to that produced by a 477 keV electron, which gives a value of $S = (477\,\text{keV})^{-1} = 2.095\,\text{MeV}^{-1}$ in the absence of electron light quenching. This is equivalent to the value of $S = 1$ MeVee/MeV used in [43]. The best-fit model in the PTB study was consistent with a quadratic coefficient, C, of zero, i.e., equivalent to the model provided in Eq. (2), although a metric directly quantifying the goodness-of-fit was not reported. In contrast, in this work, a nonzero quadratic coefficient is preferred. The Birks constant extracted in the PTB study, $kB = 9.8$ cm/GeV, is larger than that found in this work, while the fixed value of S is smaller (though consistent to within $1\,\sigma$). As the S and kB parameter errors are positively correlated, a decrease in the estimate of S would result in a decreased estimate of kB for the same predicted light yield. Hence, fixing $S = 2.095\,\text{MeV}^{-1}$ in for this work would result in a smaller value of kB for the

Table 5 Light yield of proton recoils, relative to a 477 keV electron, in 5% WbLS, and associated uncertainties (from left to right): statistical uncertainty, uncertainty on reference charge, and total uncertainty including systematic effects. A correlation matrix of the per-bin uncertainties is available upon request

Energy range [MeV]	Relative LY	Stat. uncertainty [%]	Ref. uncertainty [%]	Total uncertainty [%]
2.00–2.25	1.51	±0.58	±2.54	±5.68
2.25–2.50	1.81	±0.45	±2.54	±5.15
2.50–2.75	2.10	±0.43	±2.54	±5.23
2.75–3.00	2.39	±0.40	±2.54	±5.05
3.00–3.25	2.71	±0.37	±2.54	±4.78
3.25–3.50	3.04	±0.37	±2.54	±4.66
3.50–3.75	3.36	±0.40	±2.54	±4.49
3.75–4.00	3.68	±0.38	±2.54	±4.45
4.00–4.50	4.17	±0.28	±2.54	±4.25
4.50–5.00	4.90	±0.29	±2.54	±4.18
5.00–5.50	5.64	±0.28	±2.54	±3.92
5.50–6.00	6.34	±0.28	±2.54	±3.90
6.00–7.00	7.45	±0.24	±2.54	±3.88
7.00–8.00	9.01	±0.24	±2.54	±3.60
8.00–9.00	10.65	±0.25	±2.54	±3.35
9.00–10.00	12.17	±0.27	±2.54	±3.39
10.00–12.00	14.51	±0.26	±2.54	±3.10
12.00–14.00	17.87	±0.32	±2.54	±3.01
14.00–16.00	21.00	±0.39	±2.54	±3.14
16.00–18.00	24.54	±0.64	±2.54	±3.05
18.00–20.00	27.89	±0.90	±2.54	±3.14

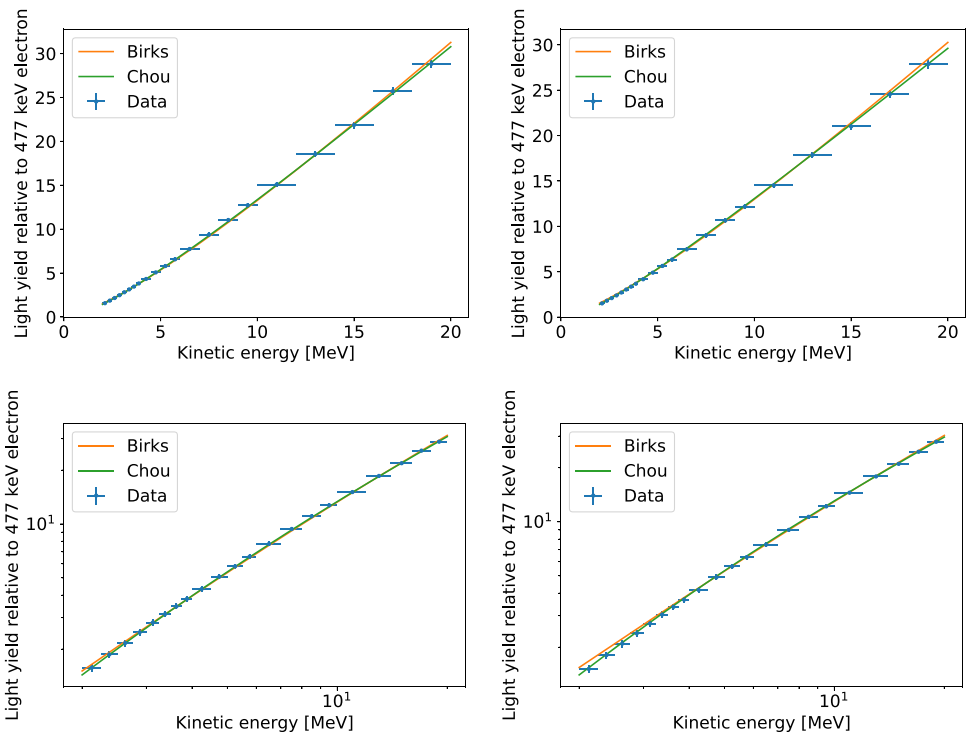

Fig. 13 Best-fit quenching models compared to the measured PLY for LABPPO (left) and WbLS (right), shown with both linear (top) and logarithmic (bottom) axes. The Birks model fails to reproduce the low-energy behavior of both materials, which is better modeled with the inclusion of the Chou bimolecular quenching term

Table 6 Best-fit model parameters for the LABPPO and WbLS proton light yields, relative to that of a 477 keV electron. Neither material is well modeled using the Birks formalism, but both are adequately described using the Chou model

	Birks		Chou	
	LABPPO	WbLS	LABPPO	WbLS
S [MeV^{-1}]	2.193 ± 0.053	2.082 ± 0.071	1.963 ± 0.074	1.776 ± 0.079
kB [cm/GeV]	7.08 ± 0.45	5.95 ± 0.43	3.76 ± 0.91	1.65 ± 0.81
C [cm^2/GeV^2]	–	–	9.88 ± 2.74	13.30 ± 2.70
χ^2/ndf	36.6/19	44.7/19	22.8/18	17.3/18

Table 7 Correlation matrices of parameter uncertainties for the Chou quenching model, in units of percent

LABPPO	S	kB	C
S	100.0	93.9	− 73.5
kB		100.0	− 87.0
C			100.0
WbLS			
S	100.0	93.7	− 70.2
kB		100.0	− 84.9
C			100.0

Birks fit, representing an even larger discrepancy with the PTB quenching parameter.

The PTB measurement extended a few hundred keV below the 2 MeV floor used in this work, but the best-fit model failed in the high energy region, systematically predicting an excess light yield above 12 MeV. Additional PLY measurements, particularly at lower energy and with deoxygenated samples, would help resolve tension with the PTB study.

4.3 Discussion

In [43], the effect of different levels of proton quenching on the detection of supernova neutrinos in large LAB-based detectors is discussed. An effective detection threshold corresponding to a 200 keV kinetic energy electron is assumed, driven by the 156 keV endpoint energy of ^{14}C β-decay, a prominent background internal to organic liquid scintillators. The relatively high degree of ionization quenching determined in that work (quantified by kB) was found to reduce the event rate in a SNO+-like detector [50] by 16% when compared to a reference quenching parameter of 7.3 cm/GeV taken from [51]. The Birks' constant extracted in this work, $kB = (7.08 \pm 0.45)$ cm/GeV, is consistent with the reference value, which restores a relatively optimistic outlook for supernova neutrino detection. Furthermore, the uniform excess in relative PLY shown in Fig. 12 translates to an increase in proton energy resolution, which would allow for a lower detection threshold and higher detection rate.

5 Conclusion

The PLY of LAB with 2 g/L PPO and 5% WbLS were measured using a double time-of-flight technique at the 88-Inch Cyclotron at Lawrence Berkeley National Laboratory. The results obtained in this work for LABPPO exposed to the atmosphere disagree with a previous measurement of deoxygenated LABPPO performed at PTB [43]. Additional measurements using both oxygenated and deoxygenated samples, ideally extending to lower proton energies, would help to resolve this discrepancy. Application of ionization quenching models revealed that neither material is adequately modeled using the Birks relation and inclusion of a bimolecular quenching term in the manner of Chou was required. These results are relevant to the design of future WbLS applications involving the detection of neutrons and protons. In the context of neutrino physics, this includes the discrimination of fast neutrons from electron-like coincidence signals, e.g., IBD events, and potential measurements of the flavor-inclusive energy spectra of neutrinos from future supernovae.

Acknowledgements The authors thank the 88-Inch Cyclotron operations and facilities staff for their help in performing these experiments. This work was performed under the auspices of the U.S. Department of Energy by Lawrence Berkeley National Laboratory under Contract DE-AC02-05CH11231. The project was funded by the U.S. Department of Energy, National Nuclear Security Administration, Office of Defense Nuclear Nonproliferation Research and Development (DNN R&D). This material is based upon work supported in part by the U.S. Department of Energy National Nuclear Security Administration through the Nuclear Science and Security Consortium under Award DE-NA0003180. EJC was funded by the Consortium for Monitoring, Technology, and Verification under Department of Energy National Nuclear Security Administration award number DE-NA0003920.

Data Availability Statement This manuscript has no associated data or the data will not be deposited. [Authors' comment: Raw data requires specialty software to be correctly analyzed; data equivalent to that presented in the detector can be offered upon request.]

Funded by SCOAP[3]. SCOAP[3] supports the goals of the International Year of Basic Sciences for Sustainable Development.

References

1. F. Reines, C.L. Cowan, Nature **178**(4531), 446 (1956). https://doi.org/10.1038/178446a0
2. F.P. An et al., Phys. Rev. Lett. **108**, 171803 (2012). https://doi.org/10.1103/PhysRevLett.108.171803
3. S. Andringa et al., Adv. High Energy Phys. **2016**, 1 (2016). https://doi.org/10.1155/2016/6194250
4. M. Yeh, S. Hans, W. Beriguete, R. Rosero, L. Hu, R.L. Hahn, M.V. Diwan, D.E. Jaffe, S.H. Kettell, L. Littenberg, Nucl. Instrum. Methods Phys. Res. Sect. A Accel. Spectrom. Detect. Assoc. Equip. **660**(1), 51 (2011). https://doi.org/10.1016/j.nima.2011.08.040
5. A.R. Back et al. arXiv:1707.08222 [physics.ins-det] (2017)
6. M. Askins et al. arXiv:1502.01132 [physics.ins-det] (2015)
7. M. Askins, Z. Bagdasarian, N. Barros, E.W. Beier, E. Blucher, R. Bonventre, E. Bourret, E.J. Callaghan, J. Caravaca, M. Diwan et al., Eur. Phys. J. C **80**(5), 416 (2020). https://doi.org/10.1140/epjc/s10052-020-7977-8
8. L.J. Bignell, D. Beznosko, M.V. Diwan, S. Hans, D.E. Jaffe, S. Kettell, R. Rosero, H.W. Themann, B. Viren, E. Worcester, M. Yeh, C. Zhang, J. Instrum. **10**(12), P12009 (2015). https://doi.org/10.1088/1748-0221/10/12/p12009
9. D.R. Onken, F. Moretti, J. Caravaca, M. Yeh, G.D. Orebi Gann, E.D. Bourret, Mater. Adv. **1**, 71 (2020). https://doi.org/10.1039/D0MA00055H
10. J. Caravaca, B.J. Land, M. Yeh, G.D. Orebi Gann, Eur. Phys. J. C **80**(9), 867 (2020). https://doi.org/10.1140/epjc/s10052-020-8418-4
11. B.J. Land, Z. Bagdasarian, J. Caravaca, M. Smiley, M. Yeh, G.D. Orebi Gann, Phys. Rev. D **103**(5), 052004 (2021). https://doi.org/10.1103/PhysRevD.103.052004
12. A. Bernstein, N. Bowden, B.L. Goldblum, P. Huber, I. Jovanovic, J. Mattingly, Rev. Mod. Phys. **92**, 011003 (2020). https://doi.org/10.1103/RevModPhys.92.011003
13. S. Yoshida, T. Ebihara, T. Yano, A. Kozlov, T. Kishimoto, I. Ogawa, R. Hazama, S. Umehara, K. Mukaida, K. Ichihara, Y. Hirano, I. Murata, J. Datemichi, H. Sugimoto, Nucl. Instrum. Methods Phys. Res. Sect. A Accel. Spectrom. Detect. Assoc. Equip. **622**(3), 574 (2010). https://doi.org/10.1016/j.nima.2010.07.087
14. W. Beriguete et al., Nucl. Instrum. Methods Phys. Res. Sect. A Accel. Spectrom. Detect. Assoc. Equip. **763**, 82 (2014). https://doi.org/10.1016/j.nima.2014.05.119
15. M.R. Anderson et al., J. Instrum. **16**(05), P05009 (2021). https://doi.org/10.1088/1748-0221/16/05/P05009
16. A. Abusleme et al., Nucl. Instrum. Methods Phys. Res. Sect. A Accel. Spectrom. Detect. Assoc. Equip. **988**, 164823 (2021)
17. J. Park et al., J. Instrum. **14**(09), T09010 (2019). https://doi.org/10.1088/1748-0221/14/09/T09010
18. M. Kireeff Covo et al., Measurement **127**, 580 (2018). https://doi.org/10.1016/j.measurement.2017.10.018
19. Eljen Technology, Neutron/Gamma PSD Liquid Scintillator EJ-301, EJ-309 (2021). https://eljentechnology.com/images/products/data_sheets/EJ-301_EJ-309.pdf
20. K.P. Harrig, B.L. Goldblum, J.A. Brown, D.L. Bleuel, L.A. Bernstein, J. Bevins, M. Harasty, T.A. Laplace, E.F. Matthews, Nucl. Instrum. Methods Phys. Res. Sect. A Accel. Spectrom. Detect. Assoc. Equip. **877**, 359 (2018). https://doi.org/10.1016/j.nima.2017.09.051
21. J.P. Meulders et al., Nucl. Instrum. Methods **126**(1), 81 (1975). https://doi.org/10.1016/0029-554X(75)90234-7
22. J. Morrell, Nex-generation iostope production via deuteron breakup. Ph.D. thesis, University of California, Berkeley (2021)
23. K.A. Weaver, J.D. Anderson, H.H. Barschall, J.C. Davis, Nucl. Sci. Eng. **52**(1), 35 (1973). https://doi.org/10.13182/NSE73-A23287
24. J.E. Bevins, Z. Sweger, N. Munshi, B. Goldblum, J. Brown, D. Bleuel, L. Bernstein, R. Slaybaugh, Nucl. Instrum. Methods Phys. Res. Sect. A Accel. Spectrom. Detect. Assoc. Equip. **923**, 79 (2019). https://doi.org/10.1016/j.nima.2019.01.049
25. J.A. Brown, B.L. Goldblum, T.A. Laplace, K.P. Harrig, L.A. Bernstein, D.L. Bleuel, W. Younes, D. Reyna, E. Brubaker, P. Marleau, J. Appl. Phys. **124**(4), 045101 (2018). https://doi.org/10.1063/1.5039632
26. J.A. Brown, A double time of flight method for measuring proton light yield. Ph.D. thesis, University of California, Berkeley (2017)
27. M. Friend, G. Franklin, B. Quinn, Nucl. Instrum. Methods Phys. Res. A Accel. Spectrom. Detect. Assoc. Equip. **676** (2011)
28. OSRAM LED Engin, High Efficiency VIOLET LED Emitter LZ1-00UB00 (2018). https://dammedia.osram.info/im/bin/osram-dam-5412887/LED%20Engin_Datasheet_LuxiGen_LZ1-00UB00_rev2.1_20181120.pdf
29. S. Agostinelli et al., Nucl. Instrum. Methods A **506**, 250 (2003). https://doi.org/10.1016/S0168-9002(03)01368-8
30. G. Dietze, H. Klein, Nucl. Instrum. Methods Phys. Res. **193**(3), 549 (1982). https://doi.org/10.1016/0029-554X(82)90249-X
31. T.A. Laplace, B.L. Goldblum, J.A. Brown, D.L. Bleuel, C.A. Brand, G. Gabella, T. Jordan, C. Moore, N. Munshi, Z.W. Sweger, A. Sweet, E. Brubaker, Nucl. Instrum. Methods Phys. Res. A **954**, 161444 (2020). https://doi.org/10.1016/j.nima.2018.10.122. (**Symposium on Radiation Measurements and Applications XVII**)
32. R. Brun, F. Rademakers, Nucl. Instrum. Methods Phys. Res. A **389**(1), 81 (1997). https://doi.org/10.1016/S0168-9002(97)00048-X
33. P. Virtanen, R. Gommers, T.E. Oliphant, M. Haberland, T. Reddy, D. Cournapeau, E. Burovski, P. Peterson, W. Weckesser, J. Bright, S.J. van der Walt, M. Brett, J. Wilson, K.J. Millman, N. Mayorov, A.R.J. Nelson, E. Jones, R. Kern, E. Larson, C.J. Carey, İ. Polat, Y. Feng, E.W. Moore, J. VanderPlas, D. Laxalde, J. Perktold, R. Cimrman, I. Henriksen, E.A. Quintero, C.R. Harris, A.M. Archibald, A.H. Ribeiro, F. Pedregosa, P. van Mulbregt, SciPy 1.0 Contributors, Nat. Methods **17**, 261 (2020). https://doi.org/10.1038/s41592-019-0686-2
34. S.G. Johnson. http://github.com/stevengj/nlopt
35. R.R. Rhinehart, R.M. Bethea, *Applied Engineering Statistics* (CRC Press, Boca Raton, 2021)
36. J.B. Birks, Proc. Phys. Soc. Sect. A **64**(10), 874 (1951). https://doi.org/10.1088/0370-1298/64/10/303
37. J. Hong, W. Craig, P. Graham, C. Hailey, N. Spooner, D. Tovey, Astropart. Phys. **16**(3), 333 (2002)
38. J.F. Williamson, J.F. Dempsey, A.S. Kirov, J.I. Monroe, W.R. Binns, H. Hedtjärn, Phys. Med. Biol. **44**(4), 857 (1999). https://doi.org/10.1088/0031-9155/44/4/004
39. T.A. Laplace, B.L. Goldblum, J.A. Brown, G. LeBlanc, T. Li, J.J. Manfredi, E. Brubaker, Mater. Adv. **3**, 5871 (2022). https://doi.org/10.1039/D2MA00388K
40. C. Chou, Phys. Rev. **87**(5), 904 (1952)
41. J.F. Ziegler, Computer program. Available at http://srim.org. Accessed Sept 2021
42. W.H. Bragg, R. Kleeman, Lond. Edinb. Dublin Philos. Mag. J. Sci. **10**(57), 318 (1905). https://doi.org/10.1080/14786440509463378

43. B. von Krosigk, L. Neumann, R. Nolte, S. Röttger, K. Zuber, Eur. Phys. J. C (2013). https://doi.org/10.1140/epjc/s10052-013-2390-1
44. I.B. Berlman, J. Chem. Phys. **34**(2), 598 (1961). https://doi.org/10.1063/1.1700992
45. J. Birks, *The Theory and Practice of Scintillation Counting. International Series of Monographs in Electronics and Instrumentation* (Pergamon Press, New York, 1964)
46. T.A. Laplace, B.L. Goldblum, J.A. Brown, J.J. Manfredi, Nucl. Instrum. Methods Phys. Res. Sect. A Accel. Spectrom. Detect. Assoc. Equip. **959**, 163485 (2020)
47. H. Wan Chan Tseung, J. Kaspar, N. Tolich, Nucl. Instrum. Methods Phys. Res. Sect. A Accel. Spectrom. Detect. Assoc. Equip. **654**(1), 318 (2011). https://doi.org/10.1016/j.nima.2011.06.095
48. R. Weldon, J. Mueller, P. Barbeau, J. Mattingly, Nucl. Instrum. Methods Phys. Res. Sect. A Accel. Spectrom. Detect. Assoc. Equip. **953**, 163192 (2020)
49. L.J. Bignell, D. Beznosko, M. Diwan, S. Hans, D. Jaffe, S. Kettell, R. Rosero, H. Themann, B. Viren, E. Worcester, M. Yeh, C. Zhang, J. Instrum. **10**(12), 12009 (2015)
50. V. Albanese, R. Alves, M. Anderson, S. Andringa, L. Anselmo, E. Arushanova, S. Asahi, M. Askins, D. Auty, A. Back et al., J. Instrum. **16**(08), P08059 (2021). https://doi.org/10.1088/1748-0221/16/08/p08059
51. B. Dasgupta, J.F. Beacom, Phys. Rev. D **83**, 113006 (2011). https://doi.org/10.1103/PhysRevD.83.113006